ISSN (Print) 1226-1750
ISSN (Online) 2233-6656
Journal of Magnetics 23(2), 160-170 (2018) https://doi.org/10.4283/JMAG.2018.23.2.160

Fast Analytical Modeling and Analysis of Flux Focusing Disk-Type Permanent Magnet Eddy Current Couplings

Dazhi Wang and Zhao Li*

School of Information Science and Engineering, Northeastern University, China

(Received 29 October 2017, Received in final form 6 April 2018, Accepted 16 April 2018)

This paper presents an improved 2-D analytical model to predict the magnetic field distributions and torque characteristics for a flux focusing disk-type permanent magnet eddy current coupling. Due to the inhomogeneous physical properties in the permanent magnet regions, based on the equivalent magnetic circuit method, a fictitious magnetization for the iron cores is introduced to simplify the complexity of modeling. The magnetic flux density distributions are derived when the eddy current generated in the copper plate and its back iron is reasonably concerned in 2-D Cartesian coordinates. Then, the explicit expression of torque is given and the torque-speed characteristics are analyzed. In the end, the calculated results of the proposed model are compared with those obtained from the magnetic equivalent circuit model and 3-D finite-element simulations.

Keywords : analytical model, magnetic field distributions, flux focusing, eddy current coupling

1. Introduction

Permanent magnet (PM) eddy current couplings can be used to transmit the torque and adjust the speed in industry [1-3]. Flux focusing disk-type PM eddy current couplings have made an alteration to the PM rotor: the circumferentially magnetized PM has a reverse polarity with its neighbor and is inserted into the iron yoke, as shown in Fig. 1. Compared with the conventional couplings with surface-mounted PM structures, they have robust rotor construction and high irreversible demagnetization withstand, which can enhance the safety and increase the productivity in the long running time [4-6]. However, the research on such devices has been insufficient, especially the accurate and simple analytical model.

At present, the flux focusing PM devices, for example, PM machines [7, 8] and PM gears [9, 10] are usually studied using the numerical approach or magnetic equivalent circuit (MEC) approach. The former, such as the finite-element method (FEM) [11-14], is mature and powerful, and acknowledged by the scholars, engineers and technicians. With this approach, the geometric details and nonlinear materials properties can be considered, thus fairly reliable results can be obtained during the analysis. However, the expensive computer resources and time-consuming procedure hinder its application in the initial design stage of such devices. Therefore, more often than not, it is employed as a means of validation. In this paper, the 3-D FEM is used to evaluate the proposed analytical model. MEC model is a simple analytical method, and has been employed for PM eddy current couplings and brakes [15-17]. But it can only offer the average values of the flux density and eddy current density, and the approximate estimation of torque. Moreover, to increase the accuracy, more magnetic circuits have to been divided, which will increase the computation of the reluctances.

The 2-D layer model has been given great attention to the study of the traditional PM eddy current couplings [18-22]. Compared with the numerical approach, its primary advantages are low computational complexity, straightforward expression form with acceptable precision. Based on some assumptions, such as linear magnetic behavior and homogeneous physical properties in each region, the model is divided into several regions, then the magnetic flux density and induced currents are derived by solving the 2-D govern equations. It is worth pointing out that some correction factors are often used to compensate the 3-D effects at last [15-23, 26]. The 3-D analytical model has recently been studied, which is extremely complex [24, 25]. Therefore, the 2-D layer model method

*Corresponding author: Tel: +86-18768800667
Fax: +86-0374-3216995, e-mail: DZWang_neu@126.com

is a good choice to predict and investigate the performances of flux focusing PM eddy current couplings. However, the homogeneous physical properties in PM region will result in complicated boundary conditions, and analytical burden [27, 28], thus the foregoing 2-D layer model cannot be used directly.

The purpose of this paper is to develop a new fully analytical model for the flux focusing disk-type PM eddy current couplings by combining MEC method with conventional 2-D layer model. The 2-D magnetic flux density, induced currents in copper plate and iron yoke, and the total torque are predicted in the proposed model. In addition, some important performances of such device are analyzed. In order to evaluate the proposed model, the analytical solutions are verified with the results obtained by the MEC method and 3-D FEM.

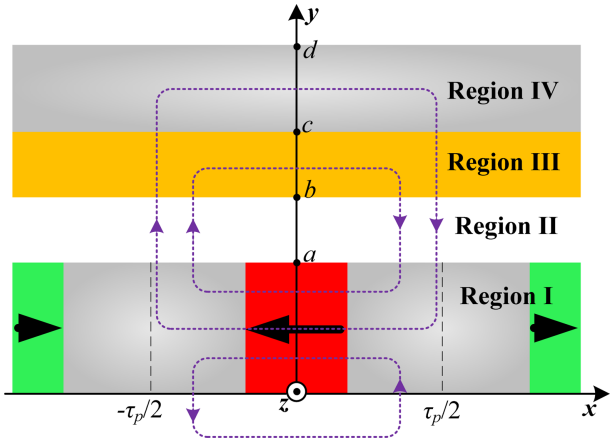

Fig. 2. (Color online) Simplified 2-D analytical model and flux paths.

2. Analytical Model

2.1. Geometry and Assumptions

The geometry of the flux focusing disk-type PM eddy current coupling is shown in Fig. 1, where the left side shows the general structure of axial-flux type, and the right sides shows the PM rotor of flux-concentration type. Table 1 illustrates the physical meaning and values of model parameters. To simplify the analysis process, the real 3-D cylindrical topology is reasonably reduced to the 2-D linear model by imaging that the structure is cut radially and rolled out circumferentially at the mean radius of the magnets [18-23]. Figure 2 shows the resulting 2-D layer model in a Cartesian coordinates (x, y, z), where the three spatial axes x, y and z indicate the circumferential, axial, and radial direction of the PM eddy current coupling, respectively. It is worth noting that Fig. 2 also depicts the flux paths which will be used to estimate the magnetization of iron poles in the subsequent section.

As shown in Fig. 2, the whole analytical domain involves four sub-regions, namely, PM with iron core region (**I**), air gap region (**II**), conductor region (**III**), and iron yoke region (**IV**). Moreover, to make the analytical solution of such motional eddy current problem simplify and rational, some assumptions are frequently performed in the modeling and analysis of the electromagnetic devices, which are adopt as follows:

(1) The conductor plate with iron yoke are stationary, and the PM rotor are moving with the translational velocity v.

(2) The iron cores of PM rotor have zero conductivity.

(3) The iron yoke have finite magnetic permeability μ_4 and nonzero conductivity σ_4, thus, this region is studied.

(4) The magnets are circumferentially magnetized with relative recoil permeability μ_r; and the permeabilities of the PMs and the conductor plate are the same as the air μ_0.

(5) The magnetic vector potential $\mathbf{A_i}$ in every region ($\mathbf{i}$ = **I**, **II**, **III**, **IV**) has only radial component (z-direction).

(6) All field quantities to be considered are periodic symmetric along the motion direction.

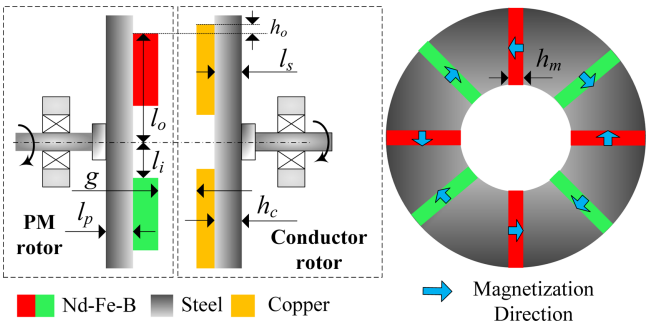

Fig. 1. (Color online) Flux focusing disk-type PM eddy-current coupling.

2.2. Problem Description and Strategy

As shown in Fig. 2, the region **I** has two different material properties, which will result in complicated boundary conditions at the interface place between PMs and iron cores. Therefore, the traditional layer model cannot be applied into the flux focusing disk-type PM eddy current coupling. In this study, to solve this problem, a fictitious magnetic source is proposed.

Due to the great relative permeability in the iron core region, most of the flux lines vertically enter the air-gap region from the iron core. Therefore, the iron cores are regarded as the field source, which must meet the follow-

Table 1. Parameters and material properties.

Symbols	Parameters	Values
l_i	Inner radius	30 mm
l_o	Outer radius	50 mm
h_m	Height of PM	5 mm
p	Pole-pairs number	4
g	Length of air-gap	1 mm
h_c	Thickness of copper plate	1 mm
l_p	Thickness of iron core	10 mm
l_s	Thickness of back iron	3.7 mm
h_o	Over length of copper plate	10 mm
B_r	Remanence of magnets	1.27 T
H_c	Coercivity of magnets	–980 kA/m
σ_3	Conductivity of copper	58 MS/m
σ_4	Conductivity of back iron	6.9 MS/m

ing requirements:

(1) The fictitious magnetic source has the same magnetic flux as the iron core, which will assure the fictitious magnetization of iron poles is proper, and the analytical model is undistorted.

(2) The fictitious magnetic source is the axially (or vertically) magnetized, and the magnetization direction is alternated from one magnet to another, which will assure the analytical model can be conveniently established.

Based on the above analysis, the fictitious magnetization of iron poles is expressed in terms of M_1. In the Cartesian coordinate system, the region **I** has been united, therefore the magnetization of region **I** can be further defined as

$$\mathbf{M} = M_x\mathbf{e}_x + My\mathbf{e}_y \tag{1}$$

where, M_x and M_y denote the horizontal component and vertical component of **M**, respectively; $\mathbf{e}_x$ and $\mathbf{e}_y$ are the unit vectors in the x- and y-directions, respectively. Figure 3 shows the distribution of M_x and M_y. Their analytical expressions in the area $x \in (-\tau_p, \tau_p)$ are given by

$$M_x = \begin{cases} -M_0, & -\tau_p < x < -\tau_p + h_m/2 \\ M_0, & -h_m/2 < x < h_m/2 \\ -M_0, & \tau_p - h_m/2 < x < \tau_p. \end{cases} \tag{2}$$

and

$$M_y = \begin{cases} -M_1, & -\tau_s - h_m/2 < x < -h_m/2 \\ M_1, & h_m/2 < x < h_m/2 + \tau_s. \end{cases} \tag{3}$$

where, τ_p is the pole pitch, and $\tau_p = h_m + \tau_s$, in addition ,we have

$$M_0 = \frac{B_r}{\mu_0} \tag{4}$$

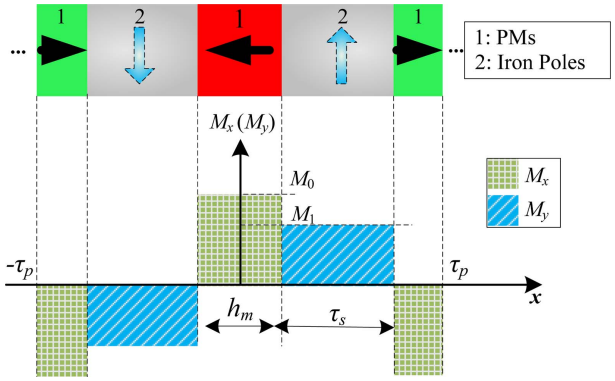

Fig. 3. (Color online) Magnetization model of PMs and iron poles.

Due to the periodicity of the field source, the magnetization can be expressed using a Fourier series with the complex notation. Therefore, (2) and (3) can be further written as

$$M_x = \sum_{n=\pm1,3,5,\cdots} \frac{2M_0}{n\pi} \sin\frac{n\pi h_m}{2\tau_p} e^{jmx} = \sum_{n=\pm1,3,5,\cdots} M_{xn} e^{jmx} \tag{5}$$

$$M_y = \sum_{n=\pm1,3,5,\cdots} \frac{2M_1}{jn\pi} \cos\frac{n\pi h_m}{2\tau_p} e^{jmx} = \sum_{n=\pm1,3,5,\cdots} M_{yn} e^{jmx} \tag{6}$$

where, n denotes the spatial harmonic number and $m = \frac{n\pi}{\tau_p}$.

2.3. Calculation of Fictitious Magnetization

The calculation of fictitious magnetization of iron poles is pretty critical. It can be determined by the assumption that the flux from an iron pole is equal to that from the surfaces of the adjacent PM without considering leaked magnetic flux. But a correction factor, which is obtained by FEM, has to be employed to compensate the deviation [29]. It is apparent that the process is cumbersome and a waste of time. In this paper, by using equivalent magnetic circuit method, a relatively accurate M_1 is derived without further correction.

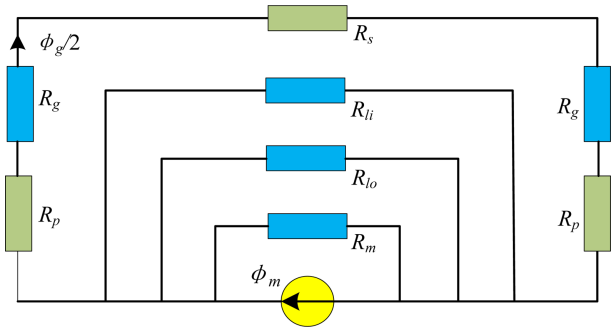

Fig. 4. (Color online) Equivalent magnetic circuit for the studied topology.

Figure 2 has shown the main flux paths, which also serve as the reference to develop the equivalent magnetic circuit in Fig. 4. By definition, in Fig. 4, φ_m is the magnetic flux of PMs; R_m is the reluctance of the PMs; R_g is the total reluctance of the air gap and conductor plate; R_p and R_s are the reluctances of the primary iron yoke and the secondary iron yoke respectively; R_{li} and R_{lo} are the reluctances corresponding to the leakage flux through the air gap and the back side of the primary iron yoke respectively. $\varphi_g/2$ is the air-gap flux that passes through one-half of the iron pole vertically. According to the relevant calculation formulas of reluctances [5, 30-32], their expressions can be easily obtained. The details are given in Appendix.

In view of no significant magnetic saturation in the iron regions, R_p and R_s can be neglected in comparison with other reluctance values [30-32]. With an analogy to Kirchoff's voltage law in circuit, φ_g is derived as

$$\phi_g = \frac{2\phi_m \times (R_{lo} \,||\, R_{li} \,||\, R_m)}{R_{lo} \,||\, R_{li} \,||\, R_m + 2R_g} \tag{7}$$

Therefore, the fictitious magnetization of iron poles can be calculated as

$$M_1 = \frac{\phi_g}{\mu_0 \tau_s (l_o - l_i)} \tag{8}$$

2.4. Flux Density Solution in Different Regions

The magnetic vector potential $\mathbf{A}(\mathbf{B} = \nabla \times \mathbf{A})$ is introduced. The field equations in different regions can be expressed in terms of **A**, subject to the Coulomb gauge, $\nabla \cdot \mathbf{A}=0$, by

$$\nabla^2 \mathbf{A_i} = \begin{cases} \mu_0(\nabla \times \mathbf{M}), & \mathbf{i=I} \\ 0, & \mathbf{i=II,V} \\ -\mu_0 \mathbf{J_{III}}, & \mathbf{i=III} \\ -\mu_4 \mathbf{J_{IV}}, & \mathbf{i=IV} \end{cases} \tag{9}$$

where, $\mathbf{J_{III}}$ and $\mathbf{J_{IV}}$ are the eddy current density induced in conductor plate and iron yoke, respectively, and given by

$$\mathbf{J_{III}} = \sigma_3 \mathbf{E_{III}} = -\sigma_3 v \frac{\partial \mathbf{A_{III}}}{\partial x} \tag{10}$$

$$\mathbf{J_{IV}} = \sigma_4 \mathbf{E_{IV}} = -\sigma_4 v \frac{\partial \mathbf{A_{IV}}}{\partial x} \tag{11}$$

where, $v = \omega R_{av}$ is the tangential speed of the conductor plate and iron yoke, where ω is the angular speed and R_{av} is the mean magnet radius.

It has been assumed that $\mathbf{A_i}$ has only z component, thus $\mathbf{A_i} = A_i(x, y)\mathbf{e}_z$, herein A_i is a scalar form, $\mathbf{e}_z$ is the unit vector in the z-direction. By using the separation of variables method, and considering the periodic distributions of the field quantities along the x-direction, the general solution of A_i in each region can be written as

$$A_I(x,y) = \sum_{n=\pm1,3,5,\cdots} e^{jmx}\left(C_{In}e^{my} + D_{In}e^{-my} + \frac{j\mu_0 M_{yn}}{m}\right) \tag{12}$$

$$A_{II}(x,y) = \sum_{n=\pm1,3,5,\cdots} e^{jmx}(C_{IIn}e^{my} + D_{IIn}e^{-my}) \tag{13}$$

$$A_{III}(x,y) = \sum_{n=\pm1,3,5,\cdots} e^{jmx}(C_{IIIn}e^{\lambda_1 y} + D_{IIIn}e^{-\lambda_1 y}) \tag{14}$$

$$A_{IV}(x,y) = \sum_{n=\pm1,3,5,\cdots} e^{jmx}(C_{IVn}e^{\lambda_2 y} + D_{IVn}e^{-\lambda_2 y}) \tag{15}$$

where,

$$\begin{cases} \lambda_1 = \sqrt[4]{m^4 + (m\mu_0\sigma_1 v)^2}\, e^{\frac{j}{2}\arctan(m^{-1}\mu_0\sigma_1 v)} \\ \lambda_2 = \sqrt[4]{m^4 + (m\mu_4\sigma_4 v)^2}\, e^{\frac{j}{2}\arctan(m^{-1}\mu_4\sigma_4 v)} \end{cases} \tag{16}$$

In order to determine the coefficients C_{In}, D_{In}, C_{IIn}, D_{IIn}, D_{IIIn}, C_{IIIn}, C_{IVn} and D_{IVn} in (12)-(15), some boundary conditions have to be satisfied. According to the continuity of the normal component of the magnetic density and the tangential magnetic field at the interface, the boundary conditions can be expressed by

$$\left.\begin{aligned} \frac{\partial A_I}{\partial x} &= \frac{\partial A_{II}}{\partial x} \\ \frac{1}{\mu_0\mu_r}\frac{\partial A_I}{\partial y} - \frac{1}{\mu_r}M_{xn} &= \frac{1}{\mu_0}\frac{\partial A_{II}}{\partial y} \end{aligned}\right|_{y=a} \tag{17}$$

$$\left.\begin{aligned} \frac{\partial A_{III}}{\partial x} &= \frac{\partial A_{II}}{\partial x} \\ \frac{\partial A_{III}}{\partial y} &= \frac{\partial A_{II}}{\partial y} \end{aligned}\right|_{y=b} \tag{18}$$

$$\left.\begin{aligned} \frac{\partial A_{III}}{\partial x} &= \frac{\partial A_{IV}}{\partial x} \\ \frac{1}{\mu_0}\frac{\partial A_{III}}{\partial y} &= \frac{1}{\mu_4}\frac{\partial A_{IV}}{\partial y} \end{aligned}\right|_{y=c} \tag{19}$$

$$\frac{1}{\mu_0\mu_r}\frac{\partial A_I}{\partial y} - \frac{1}{\mu_r}M_{xn} = 0\,|_{y=0} \tag{20}$$

$$\frac{\partial A_{IV}}{\partial x}\,|_{y=d} = 0 \tag{21}$$

where, $a = l_p$, $b = l_p+g$, $c = l_p+g+h_c$, and $d = l_p+g+h+l_s$. It's important to note that, due to the tangential component of the magnetization of the magnetic source, the magnetic field intensity of PM region can be given by

$$\mathbf{H} = \frac{B_x - \mu_0 M_x}{\mu_0\mu_r}\mathbf{e}_x + \frac{B_y - \mu_0 M_y}{\mu_0\mu_r}\mathbf{e}_y \tag{22}$$

As a matter of fact, (17) and (20) are formulated based on (22). According to the relationship between magnetic flux density and vector magnetic potential, the tangential and axial components of the magnetic flux density in every layer can be deduced by

$$\mathbf{B}_i = B_{i,x}\mathbf{e}_x + B_{i,y}\mathbf{e}_y \tag{23}$$

where,

$$B_{i,x} = \frac{\partial A_i}{\partial y},\ B_{i,y} = -\frac{\partial A_i}{\partial x} \tag{24}$$

To be emphasized, in this study, the equivalent permeability of iron yoke (μ_4) is employed with reference [33]. The corresponding formulas are presented in Appendix. When solving the coefficients C_{In}, D_{In}, C_{IIn}, D_{IIn}, D_{IIIn}, C_{IIIn}, C_{IVn} and D_{IVn}, eight linear equations are formed, which can be expressed in the matrix form. Then the solutions can be easily obtained by using the mathematical software MATLAB.

The system of linear equations can be written by

$$\mathbf{KX} = \mathbf{N} \tag{25}$$

where, **K**, **X**, and **N** denote the constant matrix, the unknown coefficient vector, and the constant column vector, respectively, and can be expressed by

$$\mathbf{X} = \left\{C_{In}, D_{In}, C_{IIn}, D_{IIn}, C_{IIIn}, D_{IIIn}, C_{IVn}, D_{IVn}\right\}^T \tag{26}$$

$$\mathbf{N} = \left\{P_1, P_2, 0, 0, 0, 0, 0, P_2\right\}^T \tag{27}$$

where,

$$P_1 = -\frac{2M_1\mu_0}{mn\pi}\cos\frac{n\pi\tau_m}{2\tau_p},\ P_2 = \frac{2M_0\mu_0}{mn\pi}sin\frac{n\pi\tau_m}{2\tau_p} \tag{28}$$

$$\mathbf{K} = \begin{bmatrix} e^{ma} & e^{-ma} & -e^{ma} & -e^{-ma} & & & & \\ e^{ma} & -e^{-ma} & -\mu_r e^{ma} & \mu_r e^{-ma} & & & & \\ & & e^{mb} & e^{-mb} & -e^{\lambda_1 b} & -e^{-\lambda_1 b} & & \\ & & me^{mb} & -me^{-mb} & -\lambda_1 e^{\lambda_1 b} & \lambda_1 e^{\lambda_1 b} & & \\ & & & & e^{\lambda_1 c} & e^{-\lambda_1 c} & -e^{\lambda_2 c} & -e^{-\lambda_2 c} \\ & & & & \mu_4\lambda_1 e^{\lambda_1 c} & -\mu_4\lambda_1 e^{-\lambda_1 c} & -\lambda_2 e^{\lambda_2 c} & \lambda_2 e^{-\lambda_2 c} \\ & & & & & & e^{\lambda_2 d} & e^{-\lambda_2 d} \\ 1 & -1 & & & & & & \end{bmatrix}^T \tag{29}$$

2.5. Electromagnetic Torque

Based on the energy conservation, an approach to calculate the total torque of the electromagnetic device is used as follows:

$$T = \frac{P}{\omega} = \frac{l_o - l_i}{\omega\sigma_3}\iint_{III}\left|J_{III}^2\right|dxdy + \frac{l_o - l_i}{\omega\sigma_4}\iint_{IV}\left|J_{IV}^2\right|dxdy \tag{30}$$

where, the right side of "=" has two parts, the torque generated by the copper plate and the iron yoke, respectively. Moreover, the eddy current can be expressed by

$$J_{III} = -jm\sigma_3 v(C_{3,n}e^{\lambda_1 y} + D_{3,n}e^{-\lambda_1 y})e^{jmx} \tag{31}$$

$$J_{IV} = -jm\sigma_4 v(C_{4,n}e^{\lambda_2 y} + D_{4,n}e^{-\lambda_2 y})e^{jmx} \tag{32}$$

2.6. 3-D Correction Factor

Though (30) can be employed to evaluate the torque characteristics, the results in magnitude will produce a large error margin [18]. The solution of eddy-current is a 3-D problem in nature, however, to simplify the analysis, it is reduced to a 2-D model. Therefore, the 3-D effects of eddy currents has been neglected in the torque expression (30). In reality, the induced currents not only flow in the *z*- direction, but also the *x*-direction that make no contribution to the transmission torque, yet produce joule loss. Among the existing correction methods, the recognized Russell and Norsworthy factor has been widely adopted in electromagnetic devices [18, 19, 26]. Therefore, the 3-D correction factor is adopted by

$$k_c = 1 - \frac{\tanh\dfrac{\pi(l_o - l_i)}{2\tau_p}}{\dfrac{\pi(l_o - l_i)}{2\tau_p}\left[1 + \tanh\dfrac{\pi(l_o - l_i)}{2\tau_p}\times\tanh\dfrac{\pi h_o}{\tau_p}\right]} \tag{33}$$

Taking the 3-D effects of the eddy current couplings into account, the total torque is further expressed by

$$T_{3-D} = k_c T \tag{34}$$

3. Valuation and Analysis

For ease of comparison studies, the geometry parameters of the studied topology listed in Table 1 are derived from the similar research in [5]. To validate the proposed analytical model, the analytical results are compared with those obtained by 3-D FEM using the software package ANSOFT Maxwell. In addition, the MEC model [5] is also applied for comparison when predicting some performances, such as the torque-slip speed characteristics. Specifically, in the analytical model, only several harmonic orders are chosen, and the 3th and 5th harmonic are considered in this paper.

3.1. 3-D Finite Element Model

The nonlinear magnetic characteristic of the back iron is considered and shown in Fig. 5. The relative permeability of copper plate is set to 1, and the other material properties are described in the Table 1.

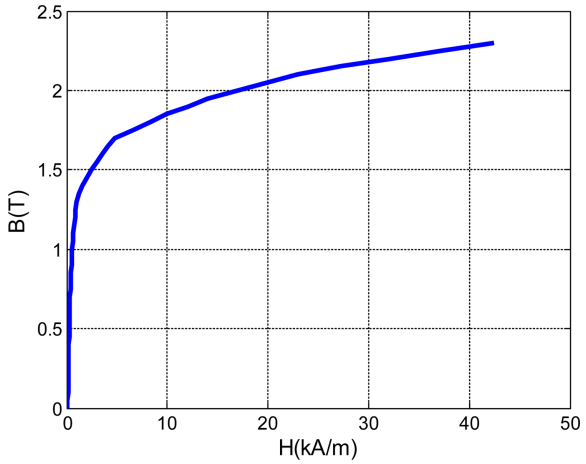

Fig. 5. (Color online) B-H curve for the ferromagnetic material.

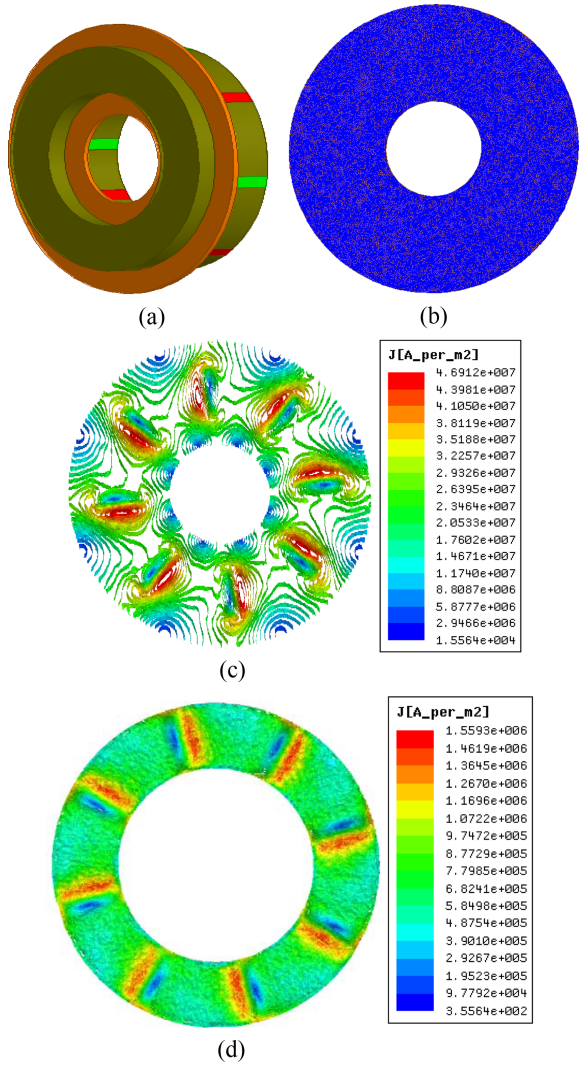

Fig. 6. (Color online) 3-D FE model. (a) 3D topology. (b) Meshing of conductor plate and back iron. (c) Current density distribution in the conductor plate. (d) Current density distribution in the iron yoke.

The 3-D finite element model of the flux focusing disk-type PM eddy current coupling is shown in Fig. 6(a). A sufficiently fine mesh of eddy current regions (conductor plate and iron yoke) is employed in Fig. 6(b). The actual current density distribution on the surface of the conductor plate and its back iron at the slip speed of 500 r/min are shown in Fig. 6(c) and (d), respectively.

It is important to note that the computation time for 3-D FEM, employing a desktop PC (32 G (RAM) with 8 core), is about 150 min (15 points), while nearly all less than 1s for the proposed analytical model.

3.2. Magnetic field distributions

Figure 7 illustrates the flux density distributions along the circumferential direction (x-direction) at the middle of air gap region, i.e. $z = a + g/2$ for two different slip speeds, namely, 0 r/min and 500 r/min. The air gap length is fixed at $g = 1$ mm. According to the corresponding calculation formulas, some parameter values are obtained. The reluctances in different region are $R_m = 1.83\times10^7$, $R_g = 3.02\times10^6$, $R_{li} = 1.54\times10^8$, $R_{lo} = 1.54\times10^7$, respectively; the fictitious magnetization is $M_1 = 4.96\times10^5$; and the coefficients of magnetic vector potential **A** are given in Table 2 and Table 3.

Thus, at the slip speed of 0 r/min, the air-gap flux density is expressed by

Table 2. Coefficients of magnetic vector potential at the relative speed of 0 r/min.

Symbols	$n = 1$	$n = 3$	$n = 5$
C_I	0.0002	0	0
D_I	–0.0017	–0.0006	–0.0003
C_{II}	0.0005	0	0
D_{II}	0.0059	0.0084	0.0247
C_{III}	0.0005	0	0
D_{III}	0.0059	0.0084	0.0247
C_{IV}	0	0	0
D_{IV}	0.0118	0.0165	0.0489

Table 3. Coefficients of magnetic vector potential at the relative speed of 500 r/min.

Symbols	$n = 1$	$n = 3$	$n = 5$
C_I	0.0002-0.0002j	0	0
D_I	–0.0017-0.0002j	–0.0006	–0.0003
C_{II}	0.0005-0.0002j	0	0
D_{II}	0.0059-0.0002j	0.0084	0.0247
C_{III}	0.0002-0.0003j	0	0
D_{III}	0.0061+0.0041j	0.0067+0.0063j	0.0186+0.0185j
C_{IV}	0	0	0
D_{IV}	0.0114-0.0020j	0.0163-0.0022j	0.0482-0.006j

$$B_{i,x\text{-}0}(x,y)=0.05e^{j100x+100y}+0.59e^{j100x-100y}-2.52e^{j300x-300y}-12.35e^{j500x-500y} \quad (35)$$

$$B_{i,y\text{-}0}(x,y)=-0.05je^{j100x+100y}-0.59je^{j100x-100y}-2.52je^{j300x-300y}-12.35je^{j500x-500y} \quad (36)$$

And at the relative speed of 500 r/min, the air-gap flux density is expressed by

$$B_{i,x\text{-}500}(x,y)=(0.05-0.02j)e^{j100x+100y}-(0.59-0.02j)e^{j100x-100y}-2.52e^{j300x-300y}-12.35e^{j500x-500y} \quad (37)$$

$$B_{i,y\text{-}500}(x,y)=-(0.02+0.05j)e^{j100x+100y}-(0.02+0.59j)e^{j100x-100y}-2.52je^{j300x-300y}-12.35je^{j500x-500y} \quad (38)$$

The parameter results may be the complex number, but only the real components are effective. It can be clearly

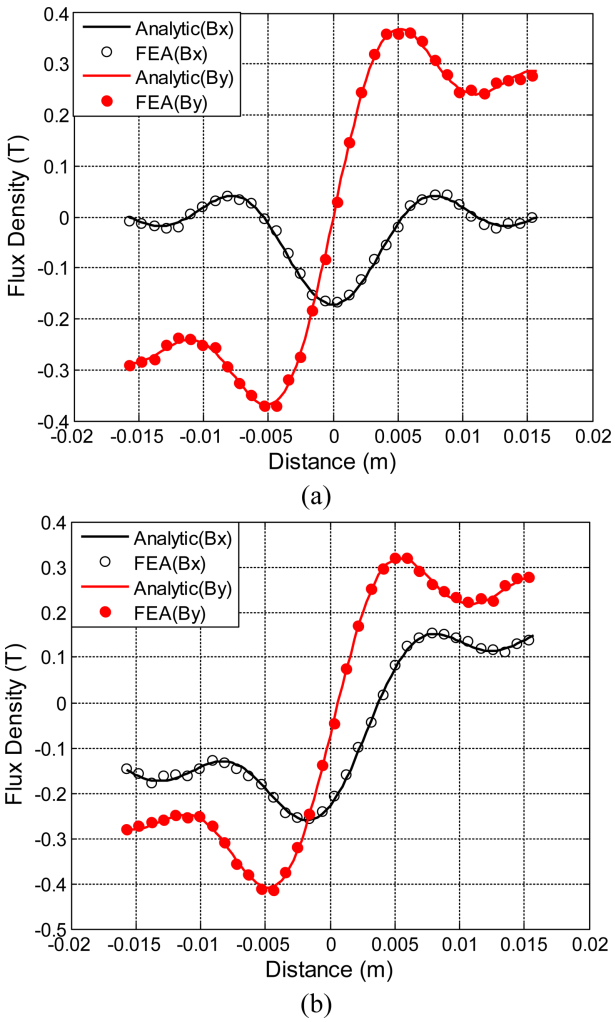

Fig. 7. (Color online) Flux density distribution along the x-direction in the middle of the air gap: (a) at a relative speed of 0 r/min. (b) at a relative speed of 500 r/min.

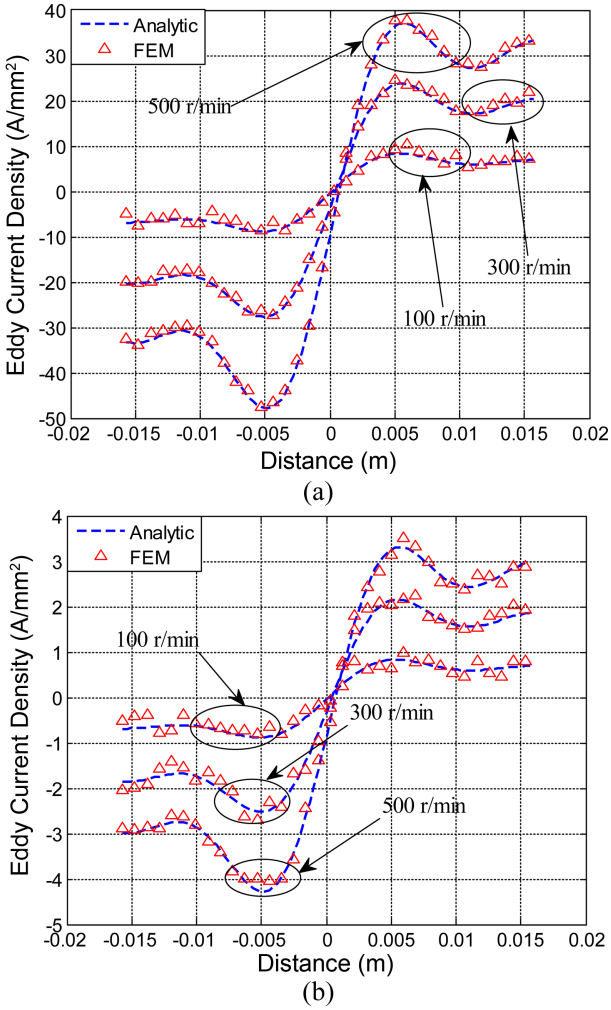

Fig. 8. (Color online) Eddy current density distribution along the *x*-direction at the surface of: (a) copper plate. (b) back iron at the relative speeds of 100 r/min, 300 r/min, and 500 r/min.

observed that the analytical results are in good agreement with the 3-D FEM simulations (FEA in Fig. 7). The slight disagreement could be down to the curvature effects and the mesh number. The curvature effects are not taken into account in the analytical model, and the mesh number will impact on the 3-D FEM results. In addition, Fig. 7 also shows that both the normal and the tangential flux density tend to be distorted due to the induced currents in conductor plate and its back iron regions.

3.3. Eddy current distributions

Figure 8 illustrates the eddy current density along the circumferential direction on the surface of copper plate and its back iron. Three different values of slip speed, namely, 100 r/min, 300 r/min and 500 r/min, are investigated, and the air-gap length is fixed at g=1 mm.

Due to the change of the slip speed, the coefficients of magnetic vector potential have changed, and Table 4 and 5 show the results. According to the analytical model, the eddy current density for the different slip speeds can be respectively expressed by

$$\begin{aligned} J_{III-100}(x,y) = {} & (1.21\times10^{7}\,j + 2.43\times10^{6})e^{(101.13+15.079j)y+j100x} \\ & +(3.643\times10^{5}\,j - 4.857\times10^{5})e^{-(101.13+15.079j)y+j100x} \\ & +(6.05\times10^{7}\,j - 9.47\times10^{6})e^{-(303.39+15.23j)y+j300x} \\ & +(2.96\times10^{8}\,j - 4.74\times10^{7})e^{-(500.23+15.242j)y+j500x} \end{aligned} \quad (39)$$

$$\begin{aligned} J_{III-300}(x,y) = {} & (2.91\times10^{6}\,j + 2.19\times10^{6})e^{(108.52+42.156j)y+j100x} \\ & +(4.37\times10^{7}\,j - 1.82\times10^{7})e^{-(108.52+42.156j)y+j100x} \\ & +(1.7\times10^{8}\,j - 8.52\times10^{7})e^{-(303.39+45.237j)y+j300x} \\ & +(8.2\times10^{8}\,j - 4.19\times10^{8})e^{-(502.07+45.56j)y+j500x} \end{aligned} \quad (40)$$

$$\begin{aligned} J_{III-500}(x,y) = {} & (2.43\times10^{6}\,j + 3.64\times10^{6})e^{(118.82+64.1710j)y+j100x} \\ & +(7.41\times10^{7}\,j - 4.98\times10^{7})e^{-(118.82+64.1710j)y+j100x} \\ & +(2.44\times10^{8}\,j - 2.29\times10^{8})e^{-(309+74.0270j)y+j300x} \\ & +(1.13\times10^{9}\,j - 1.12\times10^{9})e^{-(505.65+75.3950j)y+j500x} \end{aligned} \quad (41)$$

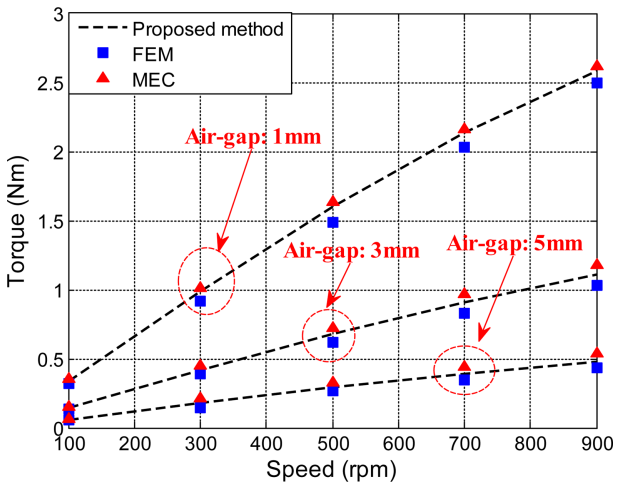

Fig. 9. (Color online) Comparison of torque-relative speed curves for different air-gap length (g = 1 mm, g = 3 mm, g = 5 mm).

Table 4. Coefficients of magnetic vector potential at the relative speeds of 100 r/min.

Symbols	$n=1$	$n=3$	$n=5$
C_I	0.0002	0	0
D_I	–0.0017	–0.0006	–0.0003
C_{II}	0.0005	0	0
D_{II}	0.0059	0.0084	0.0247
C_{III}	0.0005-0.0001j	0	0
D_{III}	0.006+0.0009j	0.0083+0.0013j	0.0244+0.0039j
C_{IV}	0	0	0
D_{IV}	0.0118-0.0004j	0.0165-0.0004j	–0.0489-0.0012j

Table 5. Coefficients of magnetic vector potential at the relative speeds of 300 r/min.

Symbols	$n=1$	$n=3$	$n=5$
C_I	0.0002	0	0
D_I	–0.0017	–0.0006	–0.0003
C_{II}	0.0005-0.0001j	0	0
D_{II}	0.0059-0.0001j	0.0084	0.0247
C_{III}	0.0004-0.0003j	0	0
D_{III}	0.006+0.0025j	0.0078+0.0039j	0.0225+0.0115j
C_{IV}	0	0	0
D_{IV}	0.0116-0.0012j	–0.0164-0.0013j	0.0486-0.0036j

It can be seen that the analytical results are accurate enough in comparison with the 3-D FEM. In addition, Fig. 8 also shows that the induced currents in back iron are far less than those in copper plate. With the increase of slip speed, the eddy current will increase, but does not exceed 50 A/mm^2, thus these working states are acceptable. Because large eddy current will cause the temperature of conductor plate rise severely.

3.4. Torque-slip speed characteristic

FigURE 9 shows the torque–slip speed characteristics obtained by the proposed model, 3-D FEM, and MEC. As shown in Fig. 9, three values for the air-gap length (g = 1 mm, g = 3 mm, and g = 5 mm) are discussed. The 3-D correction factor greatly depends on the structure parameters, therefore, for the case shown in Table 1, k_c is 0.518. Due to the change of the air gap length, the fictitious magnetization has changed, respectively, M_1 = 3.55×10^5 for g = 3 mm, and M_1 = 2.79×10^5 for g = 5 mm.

It can be seen that the predictions from the proposed model and MEC model conform with 3-D FEM results at a small gap length (g = 1 mm). However, with the increase

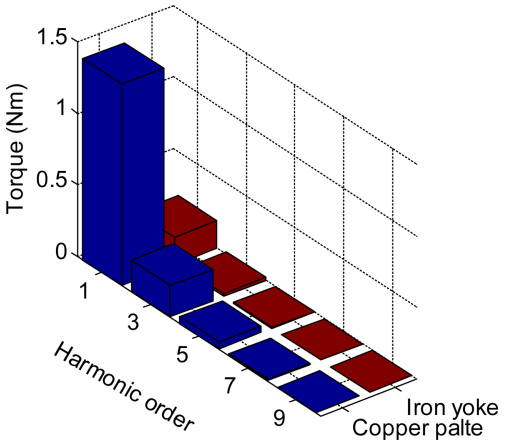

Fig. 10. (Color online) Harmonic analysis of analytical torque at a relative speed of 500 r/min.

of air gap length, the significant discrepancy between MEC and 3-D FEM appears. It is satisfying that this phenomenon does not arise in the proposed analytical model. Hence, as mentioned earlier, when MEC approach is employed to analyze and predict the performance of such devices with a large air gap length, the results are no longer reliable. In addition, one of the most outstanding feature of eddy current couplings can also be observed that adjusting the air gap length can change the output torque. Thus, such devices are also employed as the speed regulating equipment in industry.

3.5. Harmonics spectrum of transmitted torque

The harmonic analysis of the analytical torque is shown in Fig. 10. It can be discovered that the fundamental harmonic component accounting for 84.3 % of the total torque gives apparent majority role in the torque transmission system. However, the second and the third largest harmonic components, i.e., 3th harmonic and 5th harmonic, contribute to about 12.66 % and 2.59 % of the total torque, respectively. Therefore, only when the 3th harmonic and 5th harmonic are considered, can the analytical model achieve the satisfactory accuracy. On the other hand, Fig. 10 also shows that the transmitted torques associated with the iron yoke are small compared to those related to the copper plate, but they should not be omitted. In the case shown in Fig. 10, the contribution of iron region accounts for 11.54 % of the total torque.

3.6. Influence of the structure parameters

As stated previously, the contribution of the back iron to the total torque has to be considered. Herein, the effects of back iron on torque will be further investigated. Figure 11 displays the torque variations versus the thickness of back iron. Three values for the thickness of back iron, namely, l_s = 2.7 mm, l_s = 3.7 mm, and l_s = 4.7 mm are explored. As can be seen from Fig. 11, with the increase of the thickness of back iron, the total torque increases, but showing a diminishing trend; the contribution of back iron to the total torque also increases, but showing a downward trend with the increase of slip speed. Therefore, in any case, we cannot turn a blind eye to the contribution of the back iron to the total torque. However, taking into account the total weight of PM eddy current coupling and its mechanical inertia, back iron usually can't be too thick.

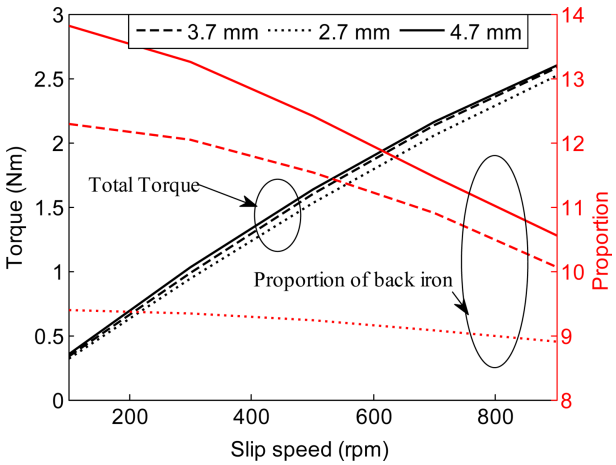

Fig. 11. (Color online) Influence of back iron yoke on the torque.

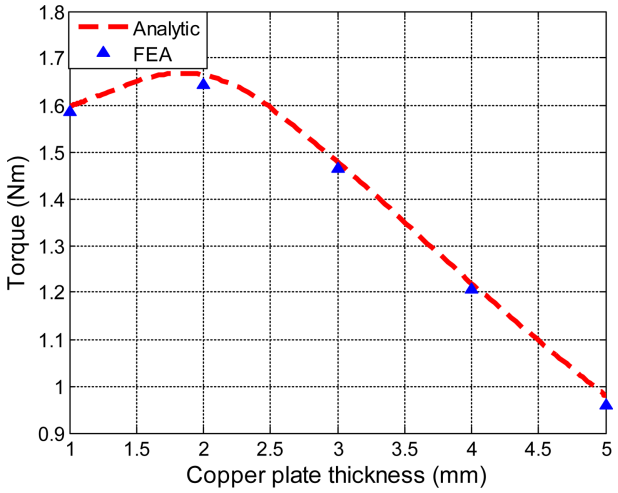

Fig. 12. (Color online) Influence of copper plate thickness on the torque.

Figure 12 shows the torque variations versus the copper thickness. The slip speed has been fixed at 500 r/min; and the other geometrical parameters remain the same. It can

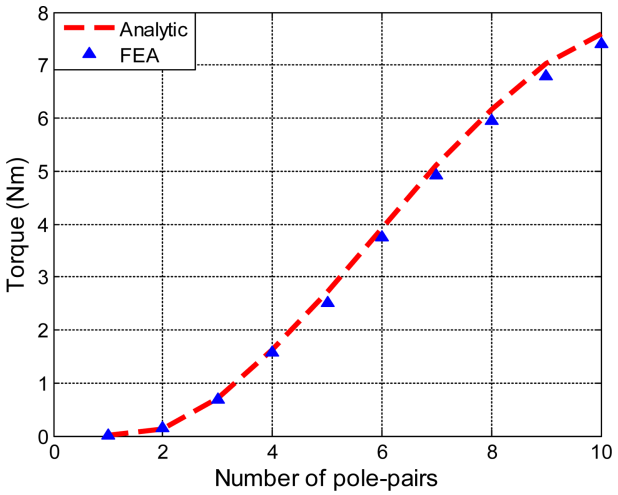

Fig. 13. (Color online) Influence of number of pole-pairs on the torque.

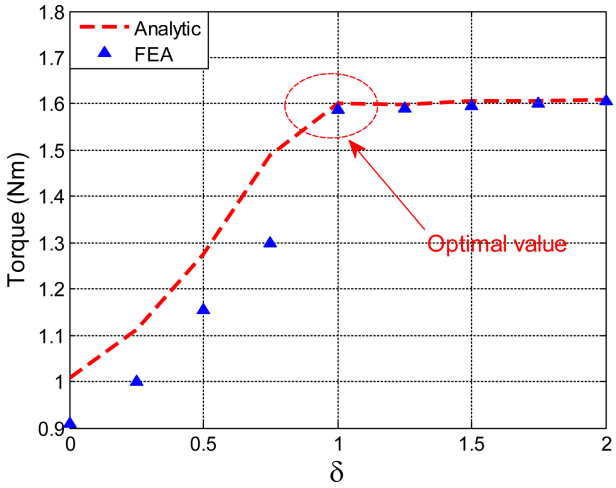

Fig. 14. (Color online) Influence of over length region of conductor plate on the torque.

be observed that an optimal value, $T \approx 1.65$ N · m for $h_c \approx 2$ mm, exists for the copper thickness in this case. Moreover, compared with the 3-D FEA, the toque formula can fairly well predict the optimal value.

The influence of the pole-pairs number on the torque is exhibited in Fig. 13. In the case, the slip speed 500 r/min is considered, and the other geometrical parameters are leave on the default values in Table 1. As can be seen from Fig. 13, with the increase of pole-pairs number, the torque will rapidly increase, but there is a converging trend for the torque curve. In addition, these values are well predicted by using the analytical model.

Because the over length part of the conductor plate can provide the return of eddy current, it is necessary to study the effect of the over length part on the torque. We have defined a dimensionless parameter δ, which shows the over length part share of the radial length of conductor plate,

$$\delta = \frac{h_o}{l_o - l_i} \tag{42}$$

Figure 14 shows the torque variations versus the value of δ. It can been observed that the torque will increase with the value of δ, and then remain steady when $\delta \geq 1$. Compared with $\delta = 0$, at the optimal condition, the torque is increased with 60 %. For the studied case (Table 1), $\delta = 1$ has been chosen. Fig. 14 also shows the δ has taken into account in the analytical model, and there is a close trend between analytical model and the 3-D FEA.

4. Conclusion

In this paper, by combining the MEC method and 2-D layer model techniques, a fully analytical model has been proposed for the flux focusing disk-type permanent magnet eddy current couplings. The prediction results of the proposed model have been validated by comparing with 3-D FEM and an existing MEC model. The model is also employed to study the harmonic and the influences of important geometrical parameters on the torque. In spite of simplicity and time-saving, the proposed model enjoys acceptable accuracy. Therefore, the analytical model is suitable in the initial design and optimization stages, and can be applicable for the other similar devices with magnetic concentration topology.

Acknowledgments

The work was supported in part by The National Key Research and Development Program of China under Grant 2017YBF1300900, in part by the National Science Foundation of China under Grant 61433004, in part by the Doctoral Scientific Research Foundation of Liaoning Province under Grant 201601030.

References

[1] A. Canova and B. Vusini, IEEE Trans. Ind. Appl. **39**, 725 (2003).
[2] H. J. Shin, J. Y. Choi, H. W. Cho, and S. M. Jang, IEEE Trans. Magn. **49**, 4152 (2013).
[3] P. J. Wyk and M. J. Kamper, IEEE Trans. Ind. Appl. **52**, 4740 (2016).
[4] L. Zhu, S. Z. Jiang, Z. Q. Zhu, and C. C. Chan, IEEE Trans. Magn. **45**, 3121 (2009).
[5] S. Mohammadi, M. Mirsalim, S. Vaez-Zadeh, and H. A. Talebi, IEEE Trans. Ind. Electron. **61**, 5940 (2014).
[6] L. Belguerras, L. Hadjout, S. Mezani, T. Lubin, and A. Rezzoug, IEEE Trans. Magn. **49**, 2291 (2013).
[7] Z. Q. Zhu, Y. Pang, D. Howe, S. Iwasaki, R. Deodhar, and A. Pride, IEEE Trans. Energy. Convers. **41**, 4277 (2005).
[8] Y. Pang, Z. Q. Zhu, D. Howe, S. Iwasaki, R. Deodhar, and A. Pride, IEEE Trans. Energy Convers. **42**, 3413 (2006).
[9] V. M. Acharya, J. Z. Bird, and M. Calvin, IEEE Trans. Magn. **49**, 4092 (2013).
[10] W. Bomela, J. Z. Bird, and V. M. Acharya, IEEE Trans. Magn. **50**, 4000104 (2014).
[11] H. J. Shin, J. Y. Choi, S. M. Jang, and K. Y. Lim, IEEE Trans. Magn. **49**, 3985 (2013).
[12] Z. Mouton and M. J. Kamper, IEEE Trans. Ind. Electron. **61**, 3367 (2014).
[13] J. Fontchastagner, T. Lubin, and D. Netter, IEEE Trans. Magn. **49**, 2291 (2013).
[14] S. E. Gay and M. Ehsani, IEEE Trans. Magn. **42**, 319

(2006).
[15] M. C. Tsai, K. Y. Chiou, S. H. Wang, and C. K. Lin, IEEE Trans. Magn. **50**, 1 (2014).
[16] S. Mohammadi, M. Mirsalim, and S. Vaez-Zadeh, IEEE Trans. Energy. Convers. **29**, 224 (2014).
[17] Y. B. Li, H. Y. Li, H. Yang, S. H. Fang, and H. B. Wang, IEEE Trans. Magn. **54**, 8000404 (2003).
[18] T. Lubin and A. Rezzoug, IEEE Trans. Ind. Electron. **6**, 2287 (2015).
[19] X. Dai, J. Cao, Y. J. Long, Q. H. Liang, J. Q. Mo, and S. G. Wang, IEEE Trans. Magn. **52**, 1 (2016).
[20] A. Canova and B. Vusini, IEEE Trans. Magn. **41**, 24 (2005).
[21] J. Wang, H. Y. Lin, and S. H. Fang, IEEE Trans. Magn. **52**, 1 (2016).
[22] M. G. Park, J. Y. Choi, H. J. Shin, and S. M. Jang, J. Appl. Phys. **115**, 17E707 (2014).
[23] X. Dai, Q. H. Liang, C. Ren, J. Y. Cao, J. Q. Mo, and S. G. Wang, J. Magn. **20**, 273 (2015).
[24] G. H. Jang, M. M. Koo, J. M. Kim, and J. Y. Choi, AIP Adv. **7**, 056647 (2017).
[25] T. Lubin and A. Rezzoug, IEEE Trans. Magn. **53**, 8002409 (2017).
[26] R. L. Russell and K. H. Norsworthy, Proc. IEE A, Power Eng. **105**, 163 (1958).
[27] S. Mezani, T. Lubin, and A. Rezzoug, IEEE Trans. Magn. **48**, 2080 (2012).
[28] F. Dubas and A. Rahideh, IEEE Trans. Magn. **50**, 1 (2014).
[29] M. G. Park, J. Y. Choi, H. J. Shin, K. Lee, and K. Hong, IEEE Trans. Magn. **50**, 1 (2014).
[30] H. K. Yeo, D. K. Lim, D. K. Woo, J. S. Ro, and H. K. Jung, IEEE Trans. Magn. **51**, 1 (2015).
[31] L. Zhu, S. Z. Jiang, Z. Q. Zhu, and C. C. Chan, IEEE Trans. Magn. **45**, 3121 (2009).
[32] M. F. Momen and S. Datta, IEEE Trans. Energy Convers. **24**, 77 (2009).
[33] J. Wang, H. Y. Lin, H. S. Li, S. H. Fang, Y. K. Huang, J. N. Dong, and H. Yang, IEEE Trans. Magn. **50**, 7002804 (2014).
[34] P. D. Agarwal, Trans. AIEE, Part I. **78**, 169 (1959).
[35] O. Biro and K. Preis, IEEE Trans. Magn. **25**, 3145 (1989).

Appendix

The elements of equivalent magnetic circuit shown in Fig. 4 are expressed by

$$\phi_m = B_r l_p (l_o - l_i) \tag{A.1}$$

$$R_m = \frac{h_m}{\mu_0 \mu_r l_p (l_o - l_i)} \tag{A.2}$$

$$R_g = \frac{g + h_c}{\mu_0 (l_o - l_i) \tau_s / 2} \tag{A.3}$$

$$R_{li} = \left[\mu_0 (l_o - l_i) \Big/ \pi \times Ln\left(1 + \pi \times (g + h_c) \Big/ h_m \right) \right]^{-1} \tag{A.4}$$

$$R_{lo} = \left[0.26 \mu_0 (l_o - l_i) + \frac{\mu_0 (l_o - l_i)}{\pi} \times Ln\left(\frac{\tau_s}{h_m} \right) \right]^{-1} \tag{A.5}$$

According to [33], the equivalent permeability of ferromagnetic materials is developed based on limiting nonlinear theory [34] and linear theory [35]. By equating the eddy current loss expressions obtained from the above two theories, the equivalent permeability μ_4 can be effectively obtained by solving the following equations

$$\frac{8}{3\pi\gamma_1} = \frac{1}{2\gamma_2} \frac{\sinh 2l_s/\gamma_2 - \sin 2l_s/\gamma_2}{\cosh 2l_s/\gamma_2 + \cos 2l_s/\gamma_2}, \gamma_1 < l_s \tag{A.6}$$

$$\frac{8}{3\pi\gamma_1}\left(1 - \left(1 - l_s^2/\gamma_1^2\right)^{\frac{3}{2}}\right) = \frac{1}{2\gamma_2} \frac{\sinh 2l_s/\gamma_2 - \sin 2l_s/\gamma_2}{\cosh 2l_s/\gamma_2 + \cos 2l_s/\gamma_2}, \gamma_1 \geq l_s \tag{A.7}$$

where,

$$\gamma_1 = \left(2H_s / \omega c_0 B_s \sigma_4 \right)^{0.5} \tag{A.8}$$

$$\gamma_2 = \left(2 / \omega \mu_4 \sigma_4 \right)^{0.5} \tag{A.9}$$

and c_0 is an empirical coefficient and set to 0.75 [33]; B_s is the peak magnetic flux density at the surface of back iroAn, H_s being the corresponding magnetic field intensity of the actual steel characteristics. It is evident that the equivalent permeability μ_4 is hidden in these equations to solve.